4-30-2012

Phase Matching for Surface Plasmon Enhanced Second Harmonic Generation in a Gold Grating Slab

Ngoc Luong
Boise State University

Cheng-Wen Cheng
Academia Sinica

Min-Hsiung Shih
Academia Sinica

Wan Kuang
Boise State University

Phase matching for surface plasmon enhanced second harmonic generation in a gold grating slab

Ngoc Luong,[1] Cheng-Wen Cheng,[2,3,4] Min-Hsiung Shih,[2] and Wan Kuang[1,a)]
[1)]*Dept. of Electrical and Computer Engineering, Boise State University, Boise, ID 83725*
[2)]*Research Center for Applied Sciences, Academia Sinica, Taipei 11529, Taiwan*
[3)]*Department of Physics, National Taiwan University, Taipei 10617, Taiwan*
[4)]*Taiwan International Graduate Program, Academia Sinica, Taipei 11529, Taiwan*

Surface plasmon enhanced second harmonic generation in gold grating slabs was investigated. The efficiency is analyzed with respect to the phase matching at the fundamental and the second harmonic frequencies. A classical electromagnetic model was developed under the weak nonlinearity approximation and solved by the finite element method. The measured zero-th order transmitted second harmonic intensity was found to be in quantitative agreement with numerical results. It is shown experimentally and numerically that proper phase matching at both frequencies improves the second harmonic efficiency.

Optical second harmonic generation (SHG) in metallic nanostructures and nanoparticles has received renewed interest lately[1,2]. In addition to producing localized electromagnetic fields, periodic arrangements of subwavelength, polarizable elements have also been shown to produce a variety of anomalous properties, such as negative refractive index[3] and zero index[4] that could result in advantageous phase matching processes not easily obtained with natural materials. Current experiments have investigated enhanced SHG due to field localization at the fundamental frequency. While high field density certainly enhances the nonlinear coefficient, an truly efficient nonlinear process also requires good phase matching.[5] In this Letter, we show numerically and experimentally that proper phase matching at both fundamental and second harmonic frequencies is important in achieving an efficient SHG.

A number of theoretical approaches[6–12] have been presented in the past for calculating nonlinear coefficients of periodic structures. Analytical[6,7,11] and semi-analytical[10,12] approaches are most suited for scenarios where a subwavelength unit cell consists of spatially slow-varying structures or the wavelengths of interest are significantly larger than the unit cell. It will be shown that a numerical method is necessary to accurately model the SHG behavior of these periodic structures since a small geometrical modification of the unit cell can have a much stronger influence on it than linear optical properties. In this Letter, a classical electrodynamic model is solved for an Au grating slab under the weak nonlinearity approximation using the finite element method (FEM). In the absence of interband transitions, the response of the conduction electrons to an external electromagnetic field may be calculated by

$$m\partial \boldsymbol{v}/\partial t + m(\boldsymbol{v}\cdot\nabla)\boldsymbol{v} = -e(\boldsymbol{E}+\boldsymbol{v}\times\boldsymbol{B}) - \boldsymbol{v}/\tau. \qquad (1)$$

Compared with a semi-classical hydrodynamic approach, this classical model ignores the contribution of electron pressure, which can be shown to have a weaker role in second harmonic generation than in photon induced voltage, another second-order nonlinearity.[13] Current density due to electron transport in the metal $\boldsymbol{J} = ne\boldsymbol{v}$ and the charge density ρ satisfy charge continuity $\partial\rho/\partial t + \nabla\cdot\boldsymbol{J} = 0$. Under the weak nonlinearity approximation, or non-depleted pump approximation, all variables in Maxwell's equations can be expanded as a series of orders where $A = A^{(1)}e^{i\omega_0 t} + A^{(2)}e^{2i\omega_0 t} + \cdots$ and A is either $\boldsymbol{E}$, $\boldsymbol{H}$, $\boldsymbol{J}$, or ρ. The vector Helmholtz equations for the fundamental frequency and the second harmonic are[14],

$$\nabla\times\nabla\times\boldsymbol{E}^{(1)} = k_0^2\varepsilon_{eff}(\omega_0)\boldsymbol{E}^{(1)} \qquad (2)$$

$$\nabla\times\nabla\times\boldsymbol{E}^{(2)} = 4k_0^2\varepsilon_{eff}(2\omega_0)\boldsymbol{E}^{(2)} + \frac{2i\omega_0\tau\mu_0}{1+2i\omega_0\tau}\boldsymbol{S}^{(2)} \qquad (3)$$

where $\varepsilon_{eff}(\omega) = \varepsilon_\infty - \omega_p^2/\left(\omega^2 - i\omega/\tau\right)$ and $\boldsymbol{S}^{(2)}$ is given by

$$\boldsymbol{S}^{(2)} = \frac{e}{m}\left(\rho^{(1)}\boldsymbol{E}^{(1)} + \boldsymbol{J}^{(1)}\times\boldsymbol{B}^{(1)}\right) + \left(\boldsymbol{J}^{(1)}\cdot\nabla\right)\boldsymbol{v}^{(1)} + \boldsymbol{v}^{(1)}\left(\nabla\cdot\boldsymbol{J}^{(1)}\right) \qquad (4)$$

Equations (2)-(3) were solved by FEM using the commercial software COMSOL[15] in the coupled multiphysics mode. The nonlinear driving force $\boldsymbol{S}^{(2)}$ is modeled as a weak contribution in COMSOL. The two-dimensional simulation was performed for a single period of an infinitely wide grating slab using a Bloch-Floquet boundary condition, port boundaries, and a perfectly matched layer boundary condition.[14] The second harmonic intensity was calculated for the Au grating slab shown in the inset of Fig. 1 as a function of wavelength and incident angle. The grating slab consists of a 50 nm thick Au film and a 3 nm thick chromium adhesion layer on a fused silica substrate. The refractive index of the substrate n_g is described by[16]

$$n_g^2 - 1 = \frac{0.696\lambda_0^2}{\lambda_0^2 - 0.068^2} + \frac{0.408\lambda_0^2}{\lambda_0^2 - 0.116^2} + \frac{0.897\lambda_0^2}{\lambda_0^2 - 9.90^2} \qquad (5)$$

in the calculation. Periodic grooves with a 1.18 μm spacing were etched into the Au film by electron beam lithography and ion beam etching.[17] The etching stopped short of completely removing the Au film to maintain electrical continuity of the grating. The calculation shows that the SHG on a two-dimensional grating slab is strictly p-polarized for p-polarized incidence. This result is consistent with analytical solutions[6,11] on a periodically corrugated metal film, which

a)Electronic mail: wankuang@boisestate.edu

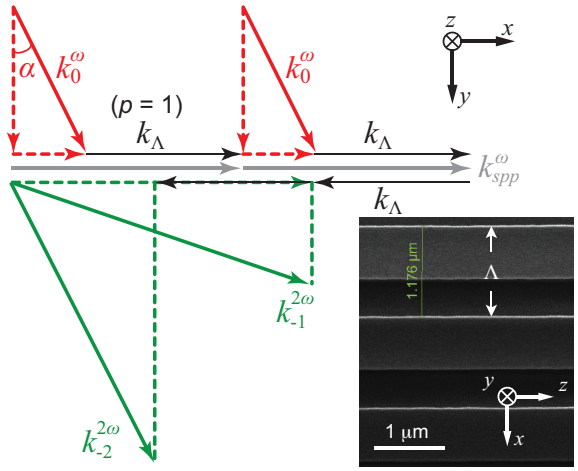

Figure 1. Vector diagram representing the phase matching conditions for various diffraction orders of SHG as a result of the excitation of surface plasmons. k_0^ω is the wave vector of the incident wave and $k_m^{2\omega}$ the SHG wave vector of the m-th order. The incident field forms an angle of α with respect to the Au grating slab. The grating grooves are oriented perpendicular to the direction of polarization. The inset shows the scanning electron microscope image of a Au grating slab. The orientations of the two graphs are indicated by the respective coordinates.

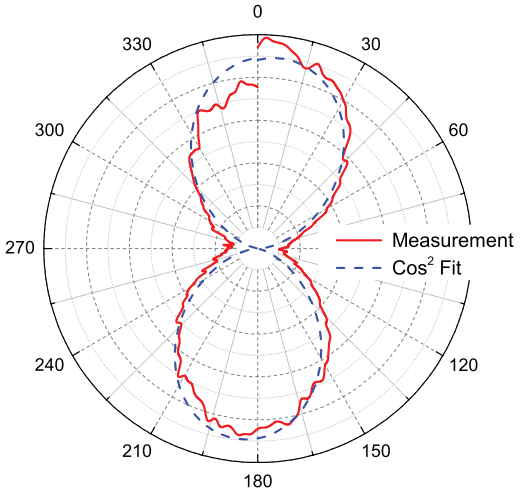

Figure 2. Measured polarization and $\cos^2$ fit of the zero-th order transmitted SHG intensity represented as a polar diagram, where 0° is oriented to the x direction as shown in Fig. 1.

shows that no s-polarized SHG exists when the excitation field is purely s- or p-polarized.

Figure 2 shows the normalized radiation intensity for the zero-th order transmitted SHG measured at the incident wavelength of 1200 nm and the incident angle of $\alpha = 32.2°$, as defined in Fig. 1. The intensity as a function of analyzer angle matches closely with the $\cos^2$ function expected for a linear polarization. In the measurements, the incident light was produced from an optical parametric amplifier (Light Conversion, TOPAS-400) pumped by the second harmonics (Light Conversion, SHBC) of a Ti:Sapphire regenerative amplifier (Coherent, Legend Elite). The wavelength was varied from 1.1 μm to 1.3 μm in the measurements. The laser beam was p-polarized and focused at the sample surface with a beam width of approximately 0.3 mm. The zero-th order transmitted light passed through a short-pass filter (Edmund Optics) and a band-pass filter (Semrock) to remove the optical power at the fundamental frequency. The SHG intensity was measured by a thermally cooled CCD camera (Princeton Instruments, ProEM 512) as a function of incident angle and wavelength. The pulse duration was 1.2 ps measured by auto-correlation, and the pulse energy was kept constant for all wavelengths at 2 μJ at the grating surface. Additionally, the transmitted SHG intensity was found to be in expected quadratic relationship with the incident power.

Figure 3 shows calculated and measured SHG intensity as well as absorbance of the Au grating slab. For the sake of clarity, results from only selected wavelengths are shown in the figure. Since the calculations were performed in the frequency domain, the results are scaled with the assumption that the pulse duration for SHG was unchanged. In addition, a transmission efficiency of 64% was assumed for the emission filters and lenses.[14] Two groups of intensity peaks can be observed in Fig. 3 – one near normal incidence and the other around the incident angle of 32°. These two groups match surface plasmon excitations at the Au-air and Au-substrate interfaces, respectively. It is clear that the measured SHG emission due to Au-air surface plasmons was significantly higher than numerical results. This behavior is due to surface contamination whose nonlinear response is enhanced by the localized electromagnetic field. It has been utilized for surface enhanced nonlinear spectroscopy[18] but will be excluded from the analysis due to the difficulty of characterizing the contaminants.

The SHG occurring on a Au grating slab can be qualitatively understood by phase matching, as illustrated by Fig. 1. Surface plasmons are excited according to the phase relation $\boldsymbol{k}_0^\omega \sin\alpha + p\boldsymbol{k}_\Lambda = \boldsymbol{k}_{spp}^\omega$ where p is an integer representing the coupling diffraction order. $k_\Lambda = 2\pi/\Lambda$ is the reciprocal lattice vector, and $\boldsymbol{k}_{spp}^\omega$ is the surface plasmon wave vector. In this experiment, the incident beam impinges on the grating slab at a direction perpendicular to the grating groove. As a result, $\boldsymbol{k}_\Lambda$, $\boldsymbol{k}_{spp}^\omega$, and $k_0^\omega \sin\alpha$ are in the same direction. Hence, the phase relation is satisfied in a scalar sense. For SHG, two photons having the same $\boldsymbol{k}_0^\omega$ produces surface plasmons of the identical $\boldsymbol{k}_{spp}^\omega$ shown as gray arrows in Fig. 1. The excited surface plasmon, in turn, radiates at the second harmonic frequency elastically under the phase matching condition $2\boldsymbol{k}_{spp}^\omega + m\boldsymbol{k}_\Lambda = \boldsymbol{k}_m^{2\omega}$, where m is an integer representing the coupling diffraction order. A number of SHG diffraction orders can be produced, two of which, $\boldsymbol{k}_{-1}^{2\omega}$and $\boldsymbol{k}_{-2}^{2\omega}$, are shown in Fig. 1. The length of $\boldsymbol{k}_m^{2\omega}$ is $2n_g\omega/c$. For transmitted SHG, diffraction orders that are totally internally reflected at the substrate air interface cannot radiate to the free space.

In comparing the SHG intensity with the absorbance shown in Fig. 3, it is clear that SHG is the strongest when the absorption is the highest. However, the difference in SHG intensity at the $\lambda_0 = 1200$ nm and 1240 nm indicates that factors

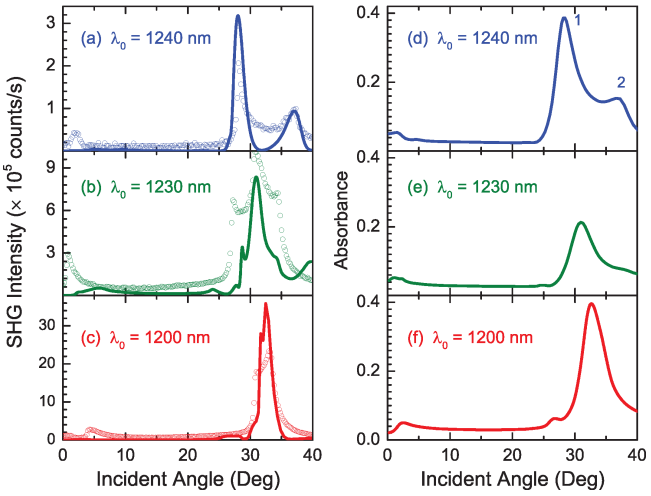

Figure 3. Calculated (curves) and measured (open circles) zero-th order transmitted SHG intensity for the Au grating slab as a function of incident angle at the wavelengths of (a) 1240 nm, (b) 1230 nm, and (c) 1200 nm. (d) - (f) calculated absorbance for the corresponding wavelengths.

other than absorption also influence SHG efficiency. At the wavelength of $\lambda_0 = 1240\,\text{nm}$, surface plasmon excitation occurs due to the diffraction orders of $p = 1$ and -2 as labeled in Fig. 3d. For the generation of zero-th order transmitted second harmonic, which has a wave vector $\boldsymbol{k}_{-2}^{2\omega}$, Fig. 1 shows that efficient coupling of surface plasmons with the reciprocal lattice vector of order $m = 2$ is required. At $\lambda_0 = 1240\,\text{nm}$, a mismatch of nearly 10° between the two diffraction orders makes the SHG process inefficient. In contrast, an order of magnitude more intense SHG can be obtained at $\lambda_0 = 1200\,\text{nm}$ when the two diffraction orders are achieved nearly simultaneously at 32°. The importance of phase matching can also be observed at $\lambda_0 = 1230\,\text{nm}$ where the SHG intensity is higher than that at 1240 nm even with lower absorption. The interactions between two diffraction orders result in multiple peaks, as observed in Fig. 3b.

From the phase matching analysis, it is expected that the zero-th order transmitted SHG intensity can be improved by increasing the strength of second-order diffraction. This can be achieved by changing the grating profile so that the incident wave is operated in the near Littrow configuration. Figure 4 compares the zero-th order transmitted SHG intensity calculated for a grating slab with a rectangular and trapezoidal groove profile under the same incident power density. The sidewall of the trapezoidal groove forms a 30° angle with the surface normal of the substrate. To focus on the issue of diffraction strength, the trapezoidal groove is made symmetric in the calculation to avoid the possibility of second harmonic enhancement due to the asymmetric distribution of the surface electromagnetic field along the grating direction. As observed in Fig. 4, a factor of 3 increase at the wavelength of 1160 nm can be obtained by simply changing the groove profile from rectangular to trapezoidal. The total transmitted SHG intensity is also increased.[14] Further investigation indicates that the two grating profiles differ little in terms of absorption which

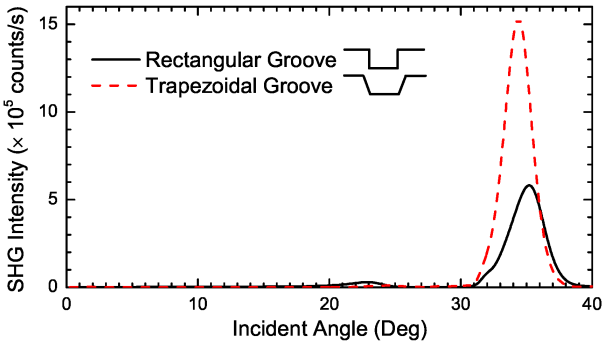

Figure 4. The calculated zero-th order transmitted SHG intensity as a function of incident angle at the incident wavelength of 1160 nm for Au grating slab with rectangular and trapezoidal groove profiles.

rules out the possibility of more efficient surface plasmon excitation. This change of SHG intensity due to a small geometrical modification of the structure indicates that a numerical, and even microscopic modeling of SHG is necessary.

In summary, surface plasmon enhanced SHG on a Au grating slab was investigated numerically and experimentally. A classical electrodynamic model was solved under the weak nonlinearity approximation and found to be in good agreement with the measurements. It was shown that proper phase matching can achieve significant improvement in SHG efficiency.

This work has been supported by grants from NSF CAREER ECCS-0846415 and NSF MRI ECCS-0923541 and by DARPA under contract N66001-01-C-80345. The authors acknowledge helpful discussions with E. Graugnard.

[1] M. W. Klein, C. Enkrich, M. Wegener, and S. Linden, Science **313**, 502 (2006).
[2] S. Tang, D. J. Cho, H. Xu, W. Wu, Y. R. Shen, and L. Zhou, Opt. Express **19**, 18283 (2011).
[3] J. Valentine, S. Zhang, T. Zentgraf, E. Ulin-Avila, D. A. Genov, G. Bartal, and X. Zhang, Nature **455**, 376 (2008).
[4] R. W. Ziolkowski, Phys. Rev. E **70**, 046608 (2004).
[5] A. Rose and D. R. Smith, Opt. Mater. Express **1**, 1232 (2011).
[6] N. Bloembergen, R. K. Chang, S. S. Jha, and C. H. Lee, Phys. Rev. **174**, 813 (1968).
[7] C. K. Chen, A. R. B. de Castro, and Y. R. Shen, Phys. Rev. Lett. **46**, 145 (1981).
[8] M. Corvi and W. L. Schaich, Phys. Rev. B **33**, 3688 (1986).
[9] Y. Zeng, W. Hoyer, J. Liu, S. W. Koch, and J. V. Moloney, Phys. Rev. B **79**, 235109 (2009).
[10] A. Rose, S. Larouche, D. Huang, E. Poutrina, and D. R. Smith, Phys. Rev. E **82**, 036608 (2010).
[11] M. Gigli, M. Inchaussandague, C. Valencia, and E. Méndez, J. Opt. Soc. Am. B **28**, 1940 (2011).
[12] Y. Zeng, D. A. R. Dalvit, J. O'Hara, and S. A. Trugman, Phys. Rev. B **85**, 125107 (2012).
[13] A. English, C.-W. Cheng, L. Lowe, II, M.-H. Shih, and W. Kuang, Applied Physics Letters **98**, 191113 (2011).
[14] See supplementary material at [URL will be inserted by AIP] for details regarding the derivations and discussions.
[15] "Multiphysics modeling and simulation software," .
[16] I. H. Malitson, J. Opt. Soc. Am. **55**, 1205 (1965).
[17] C.-W. Cheng, M. N. Abbas, M.-H. Shih, and Y.-C. Chang, Opt. Express **19**, 23698 (2011).
[18] G. C. Schatz and R. P. Van Duyne, "Electromagnetic mechanism of surface-enhanced spectroscopy," in *Handbook of Vibrational Spectroscopy* (John

Wiley & Sons, Ltd, 2006).

Phase matching for surface plasmon enhanced second harmonic generation in a gold grating slab

Ngoc Luong and Wan Kuang*

Dept. of Electrical and Computer Engineering,

Boise State University, Boise, ID 83725

Cheng-Wen Cheng

Research Center for Applied Sciences,

Academia Sinica, Taipei 11529, Taiwan and

Department of Physics, National Taiwan University, Taipei 10617, Taiwan

Min-Hsiung Shih

Research Center for Applied Sciences,

Academia Sinica, Taipei 11529, Taiwan

*Electronic address: wankuang@boisestate.edu

The supplemental material includes finite element modeling with COMSOL using multi-physics model and more detailed results not shown in the manuscript.

I. COMSOL MODELING

The vector Helmholtz equations with respect to $\boldsymbol{E}$ for the fundamental frequency and the second harmonic are [1]

$$\nabla \times \nabla \times \boldsymbol{E}^{(1)} = k_0^2 \left(\varepsilon_\infty - \frac{\omega_p}{\omega_0^2 - i\omega_0/\tau} \right) \boldsymbol{E}^{(1)} \tag{1}$$

$$\nabla \times \nabla \times \boldsymbol{E}^{(2)} = 4k_0^2 \left(\varepsilon_\infty - \frac{\omega_p^2}{4\omega_0^2 - 2i\omega_0/\tau} \right) \boldsymbol{E}^{(2)} + \frac{2i\omega_0\tau\mu_0}{1+2i\omega_0\tau} \boldsymbol{S}^{(2)} \tag{2}$$

$$= k_0^2 \left(4\varepsilon_\infty - \frac{2\omega_p^2}{2\omega_0^2 - i\omega_0/\tau} \right) \boldsymbol{E}^{(2)} + \frac{2i\omega_0\tau\mu_0}{1+2i\omega_0\tau} \boldsymbol{S}^{(2)} \tag{3}$$

$$= k_{(2)}^2 \left(\varepsilon_\infty - \frac{\omega_p^2}{\omega_{(2)}^2 - i\omega_{(2)}/\tau} \right) \boldsymbol{E}^{(2)} + \frac{i\omega_{(2)}\tau\mu_0}{1+i\omega_{(2)}\tau} \boldsymbol{S}^{(2)} \tag{4}$$

In the Cartesian coordinate, the nonlinear driving force $\boldsymbol{S}^{(2)}$ can be written as,

$$\begin{aligned}
\boldsymbol{S}^{(2)} = & \frac{e\rho^{(1)}}{m} \left(E_x^{(1)}\hat{x} + E_y^{(1)}\hat{y} + E_z^{(1)}\hat{z} \right) \\
& + \frac{e}{m} \left[\left(J_y^{(1)} B_z^{(1)} - J_z^{(1)} B_y^{(1)} \right) \hat{x} + \left(J_z^{(1)} B_x^{(1)} - J_x^{(1)} B_y^{(1)} \right) \hat{y} + \left(J_x^{(1)} B_y^{(1)} - J_y^{(1)} B_x^{(1)} \right) \hat{z} \right] \\
& + \left[\left(J_x^{(1)} \frac{\partial}{\partial x} + J_y^{(1)} \frac{\partial}{\partial y} + J_z^{(1)} \frac{\partial}{\partial z} \right) v_x^{(1)} + v_x^{(1)} \left(\frac{\partial J_x^{(1)}}{\partial x} + \frac{\partial J_y^{(1)}}{\partial y} + \frac{\partial J_z^{(1)}}{\partial z} \right) \right] \hat{x} \\
& + \left[\left(J_x^{(1)} \frac{\partial}{\partial x} + J_y^{(1)} \frac{\partial}{\partial y} + J_z^{(1)} \frac{\partial}{\partial z} \right) v_y^{(1)} + v_y^{(1)} \left(\frac{\partial J_x^{(1)}}{\partial x} + \frac{\partial J_y^{(1)}}{\partial y} + \frac{\partial J_z^{(1)}}{\partial z} \right) \right] \hat{y} \\
& + \left[\left(J_x^{(1)} \frac{\partial}{\partial x} + J_y^{(1)} \frac{\partial}{\partial y} + J_z^{(1)} \frac{\partial}{\partial z} \right) v_z^{(1)} + v_z^{(1)} \left(\frac{\partial J_x^{(1)}}{\partial x} + \frac{\partial J_y^{(1)}}{\partial y} + \frac{\partial J_z^{(1)}}{\partial z} \right) \right] \hat{z}
\end{aligned}$$

or

$$\begin{aligned}
S_x^{(2)} = & \frac{e}{m} \left(\rho^{(1)} E_x^{(1)} + J_y^{(1)} B_z^{(1)} - J_z^{(1)} B_y^{(1)} \right) \\
& - \frac{1}{en_0} \left(J_x^{(1)} \frac{\partial J_x^{(1)}}{\partial x} + J_x^{(1)} \frac{\partial J_x^{(1)}}{\partial x} + J_y^{(1)} \frac{\partial J_x^{(1)}}{\partial y} + J_x^{(1)} \frac{\partial J_y^{(1)}}{\partial y} + J_z^{(1)} \frac{\partial J_x^{(1)}}{\partial z} + J_x^{(1)} \frac{\partial J_z^{(1)}}{\partial z} \right)
\end{aligned} \tag{5}$$

$$\begin{aligned}
S_y^{(2)} = & \frac{e}{m} \left(\rho^{(1)} E_y^{(1)} + J_z^{(1)} B_x^{(1)} - J_x^{(1)} B_z^{(1)} \right) \\
& - \frac{1}{en_0} \left(\frac{\partial J_x^{(1)} J_y^{(1)}}{\partial x} + \frac{\partial J_y^{(1)} J_y^{(1)}}{\partial y} + \frac{\partial J_y^{(1)} J_z^{(1)}}{\partial z} \right)
\end{aligned} \tag{6}$$

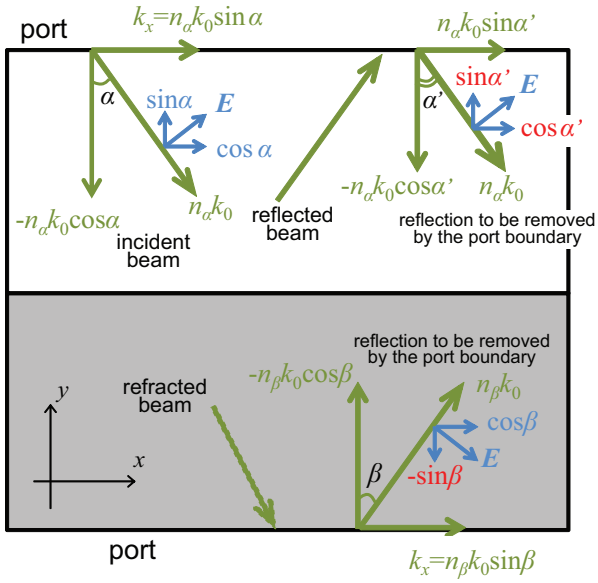

Figure 1: Schematic for setting up COMSOL port boundary.

$$S_z^{(2)} = \frac{e}{m}\left(\rho^{(1)}E_z^{(1)} + J_x^{(1)}B_y^{(1)} - J_y^{(1)}B_x^{(1)}\right) + \frac{1}{en_0}\left(\frac{\partial J_x^{(1)}J_z^{(1)}}{\partial x} + \frac{\partial J_y^{(1)}J_z^{(1)}}{\partial y} + \frac{\partial J_z^{(1)}J_z^{(1)}}{\partial z}\right) \tag{7}$$

The form of the equation for electric field Helmholtz equations, Eqs. (1) and (2), is somewhat simpler than that for the magnetic fields. The two Helmholtz equations (1) and (4) are solved by two COMSOL models referred to as `emw1` and `emw2` in the following context. `emw1` is for the field propagation at the fundamental frequency and `emw2` for the electromagnetic radiation at the second harmonic. The two models are coupled by $\boldsymbol{S}^{(2)}$ as shown in Eq. (4). For the `emw1` model, it is set up for one unit cell of the grating slab with Bloch-Floquet boundary conditions describing the periodicity. The condition states that the solution on one side of the unit equals the solution on the other side multiplied by a complex-valued phase factor. The phase shift between the boundaries is evaluated from the component of the wave vector perpendicular to the Bloch-Floquet boundaries. Because the periodic boundaries are parallel with the y-axis, only the x-component is required. For a plane wave incidence, the phase shift between the Bloch-Floquet boundaries also determines the incident angle. It shall be noted that the phase factor for the refracted and reflected beams is the same as for the incident wave due to the continuity of the field. The `emw1` model computes transmittance and reflectance for the refraction, specular reflection, and diffractions.

$\cos\alpha' \exp\left(-in_\alpha k_0 \sin\alpha' x\right)$	x
$\sin\alpha' \exp\left(-in_\alpha k_0 \sin\alpha' x\right)$	y
0	z

Table I: Port mode settings for reflected diffracted beams. n_α is the refractive index of the incident medium, α' is the angle of diffraction for the m-th order given by $\cos\alpha' = \left(n_\alpha k_0 \sin\alpha + mk_\Lambda\right)/n_\alpha k_0$.

$\cos\beta \exp\left(-in_\beta k_0 \sin\beta x\right)$	x
-$\sin\beta \exp\left(-in_\beta k_0 \sin\beta x\right)$	y
0	z

Table II: Port mode settings for transmitted diffracted beams. n_β is the refractive index of the transmitted medium, β is the angle of diffraction for the m-th order given by $\cos\beta = \left(n_\alpha k_0 \sin\alpha + mk_\Lambda\right)/n_\beta k_0$.

The top and bottom boundaries of the calculation domain are terminated by port boundaries. Port conditions are used both for specifying the incident wave and for the scattering field leaving the domain without any non-physical reflections. To achieve perfect transmission through the port boundaries, one port for each mode ($p = 0$, $p = -1$, $p = 1$, etc) in each direction must be present. The input to each port condition is an electric field vector and a propagation constant. The electric field describes the specular reflection of the mode that the port should transmit, as shown in Fig. 1. This convention makes it possible to have the input port automatically transmit the specular reflection of the incident wave. The propagation constant is the component along the outwards-facing normal, which should be positive for all transmitted waves. For reflected diffracted beams, the port mode settings are shown in Table I. For transmitted diffracted beams, the port mode settings are shown in Table II. A total of 3 and 5 ports are defined for the top and bottom boundaries, respectively.

The periodic boundary conditions require the mesh to be identical on the boundaries when dealing with vector degrees of freedom, as is the case in the TM mode propagation. This is accomplished by copy edge meshes of the corresponding boundaries. Since the electromagnetic field is localized at and near the Au film, it is desirable to increase the mesh density accordingly. This is particularly important for the `emw2` model because a smaller mesh size is necessary to properly calculate the spatial derivatives of the electromagnetic

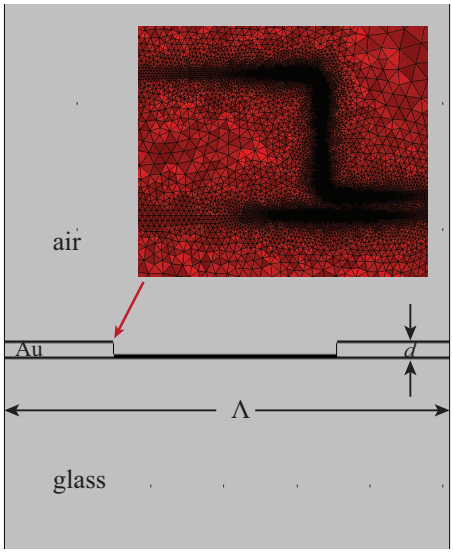

Figure 2: The structure employed in COMSOL modeling. The inset shows an increased mesh density near the edge of the groove.

field required by the nonlinear driving force $\boldsymbol{S}$. In this calculation, both `emw1` and `emw2` models share the same mesh. A maximal mesh size of 0.2 nm is enforced around the edges of the grating groove, as shown in Fig. 2. To avoid the computational difficulty with the field localization at sharp corners, the edges of the grating groove is fillet by a polyline with an effective radius of 5 nm.

For the `emw2` model, the calculation is also performed on the same unit cell of the grating slab with Bloch-Floquet boundary condition. Due to the conservation of momentum, the phase factor for the `emw2` model shall be twice of that defined for the `emw1` model. In order to couple the solution from the `emw1` model, a weak contribution, $S_x * \text{test}\left(E_x^{(2)}\right) + S_y * \text{test}\left(E_y^{(2)}\right) + S_z * \text{test}\left(E_z^{(2)}\right)$, is added to the otherwise source-less Helmholtz equation. Since the generated electric field consists of all vector components in general, the modeling of SHG will be performed on three-component Helmholtz equation rather than on TE or TM field separately. As a result, defining port boundaries for the `emw2` model is not practical. Instead, perfectly matched layers (PMLs) are added to the top and bottom of the calculation domain to allow the field radiating out of the domain without reflection. The reflected and transmitted SHG intensity for each diffraction order is calculated by projecting the solution to a sum of plane wave solutions. For the TM mode, the electric field consists of a scalar quantity $E_z(x, y)$. In a periodic structure, the field at any given y_0 can be written as a sum

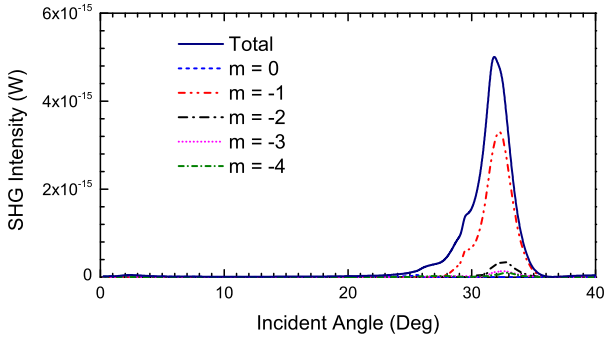

Figure 3: Calculated transmitted SHG intensity as a function of incident angle for various diffraction orders.

of spatial harmonics,

$$E_z(x) = \sum_m c_m e^{-ik_x^{(m)}x} = \sum_m c_m e^{-ik_x^{(0)}x} e^{-i\frac{2m\pi}{\Lambda}x} \tag{8}$$

where

$$c_m = \frac{1}{\Lambda}\int_0^\Lambda E_z e^{ik_x^{(m)}x} dx \tag{9}$$

The power density for each spatial harmonic is a constant, given by

$$S_m = \frac{1}{2} Z_0 |c_m|^2 \tag{10}$$

where Z_0 is the impedance of the medium. The power density assumes the direction of $\left(k_x^{(m)}\hat{x} + k_z^{(m)}\hat{z}\right)/k_0$. The total power carried by each spatial harmonic for a period is

$$P_m = \frac{k_z^{(m)} Z_0}{2k_0\Lambda}\int_0^\Lambda E_z e^{ik_x^{(m)}x} dx \tag{11}$$

Figure 3 shows the transmitted SHG intensity as a function of incident angle for different diffraction orders. The zero-th transmitted SHG intensity has a diffraction order of $m = -2$.

Equations (1)-(4) applies to both dielectric and metallic materials. For metallic materials, it is described by plasmon frequency ω_p and plasmon lifetime τ in addition to its nondispersive dielectric constant ε_∞. The nondispersive dielectric constant is a fitting parameter to minimize the difference between the Drude model and the measured dielectric constant of the metal. In practice, the dielectric constant of a metal is affected by many factors, such as, surface preparation and deposition method. Drude model is only a very

crude approximation of its optical properties. For Au, the following parameters are used in simulation

$$\omega_p = 1.367 \times 10^{16}\,\mathrm{rad/s} \tag{12}$$

$$\tau = 1.544 \times 10^{-14}\,\mathrm{s} \tag{13}$$

$$\varepsilon_\infty = 1 \tag{14}$$

after the reference [1]. For dielectric media, the materials possess an effective lifetime $\tau = 0$. Hence without the presence of metal, Eqs. (1) and (2) decouple. It indicates that the classical model derived herein produces zero nonlinear effect without the existence of surface plasmon resonance.The computation is performed with frequency domain analysis in the 2D electromagnetic wave module (radio frequency). In principle, the frequency of the incident electromagnetic wave can be specified by `freq` directly. But for SHG calculation where the wavelengths at the fundamental frequency and the second harmonics need to be swept in tandem, it would be more convenient to define a parametric sweep step. The sweep parameter in the parametric sweep step is selected from the constants defined in the global parameters section. By default, COMSOL solves the two sets of equations simultaneously. Since Eq. (1) and Eq. (2) are decoupled under the weak nonlinearity approximation, the two equations are to be solved sequentially in COMSOL. This requires creating a new COMSOL study for Eq. (2) and remove the same equation from the original study that COMSOL automatically creates.

II. RESULTS

The calculation was performed in the frequency domain for a single period of the grating slab, as shown in Fig. 2. Hence, the numerical results needed to be scaled in order to compare with the measurement. Using the port boundary, the calculation assumed a power of 1 W for the incident plane wave. For 2D modelings, COMSOL assumes the third dimension (in the z direction) to be 1 m. As a result, the incident power density is

$$S_n = \frac{1\mathrm{W}}{1\mathrm{m} \times 1.18\mu\mathrm{m}} \approx 84.7\mathrm{W/cm}^2$$

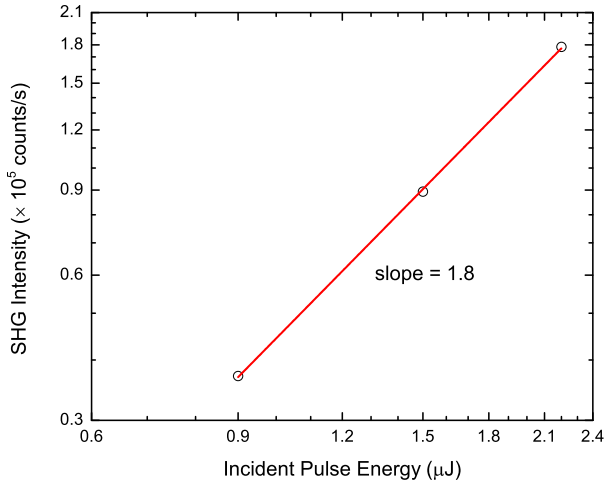

Figure 4: Transmitted zero-th order SHG intensity versus incident laser power on a log-log scale measured at 1240 nm. The straight line is a fit to the measurement and has a slope of 1.8.

It is obvious that this power density is much lower than that employed in the experiments, which can be estimated by

$$S_e = \frac{2\mu\text{J}/1.2\text{ps}}{\pi \times (0.03\text{cm})^2} \approx 0.6\text{GW/cm}^2$$

Because SHG intensity is quadratically related to the incident power density for classical electromagnetic calculations, the calculated SHG power density can be simply scaled by $(S_e/S_n)^2$ for the incident power employed in the experiments. As a result, the calculated SHG intensity is the product of the scaled power density, the device area ($350\,\mu\text{m} \times 400\,\mu\text{m}$), and the pulse duration.

A. SHG intensity v.s. incident power

The SHG intensity as a function of incident pulse energy is shown in Fig. 4 for Au grating slab at the wavelength of 1240 nm. It cab be seen that SHG intensity maintains a nearly quadratic relationship with the incident power, as expected for SHG.

B. SHG by Trapezoidal Grating

For Au grating slabs with rectangular and trapezoidal groove profiles, the calculations showed that the two gratings differ little in terms of absorption, as shown in Fig. 5. It

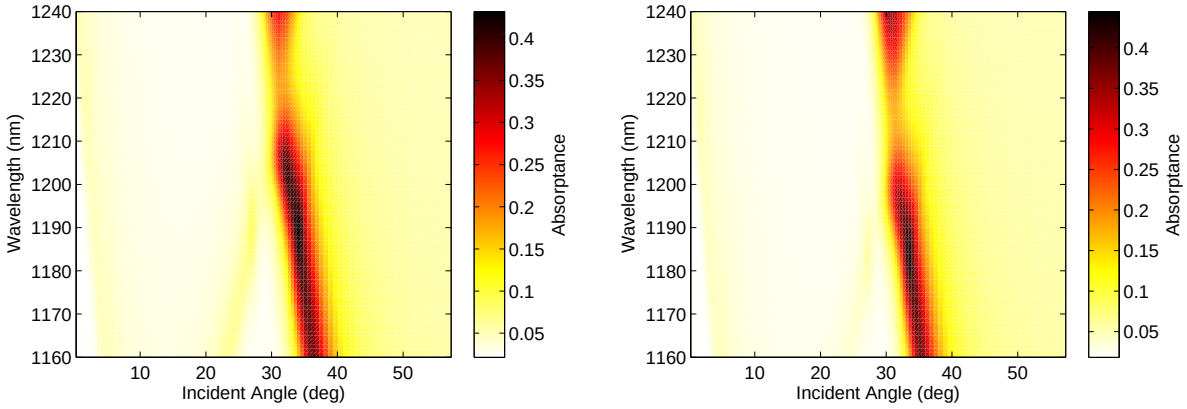

(a) (b)

Figure 5: The absorptance as a function of incident angle and incident wavelength for Au grating slab with (a) rectangular and (b) trapezoidal groove profiles.

suggests that the enhanced zero-order transmitted SHG intensity is not due to an increased absorption. The degenerate resonant frequency for trapezoidal grating is approximately 5 nm blue-shifted than the rectangular grating, suggesting a subtle change in surface electromagnetic modes.

As a result of the resonance frequency shift due to different grating profile, the transmitted zero-th order SHG intensity also displays a similar frequency shift. In Fig. 6, the zero-th order transmitted SHG intensity is shown as a function of incident angle and wavelength for both groove profiles. Even though the calculation is not performed for the wavelength shorter than 1160 nm, it is clear that peak SHG intensity is achieved over a broader wavelength range for trapezoidal grating slab.

Finally, the total transmitted SHG intensity as a function of incident angle and wavelength is calculated for grating slabs of both groove profiles. This includes SHG intensity of all propagating diffraction orders. Figure 7 shows that the total SHG intensity is enhanced by the change of groove profile but to a smaller extent than the zero-th order transmitted SHG intensity.

[1] Y. Zeng, W. Hoyer, J. Liu, S. W. Koch, and J. V. Moloney, Phys. Rev. B **79**, 235109 (2009).

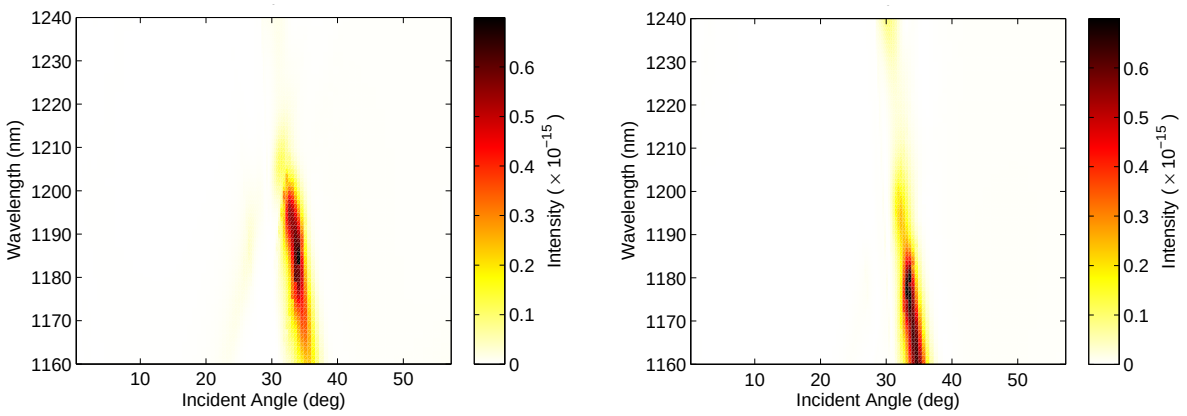

(a) (b)

Figure 6: The zero-th order transmitted SHG intensity as a function of incident angle and incident wavelength for Au grating slab with (a) rectangular and (b) trapezoidal groove profiles.

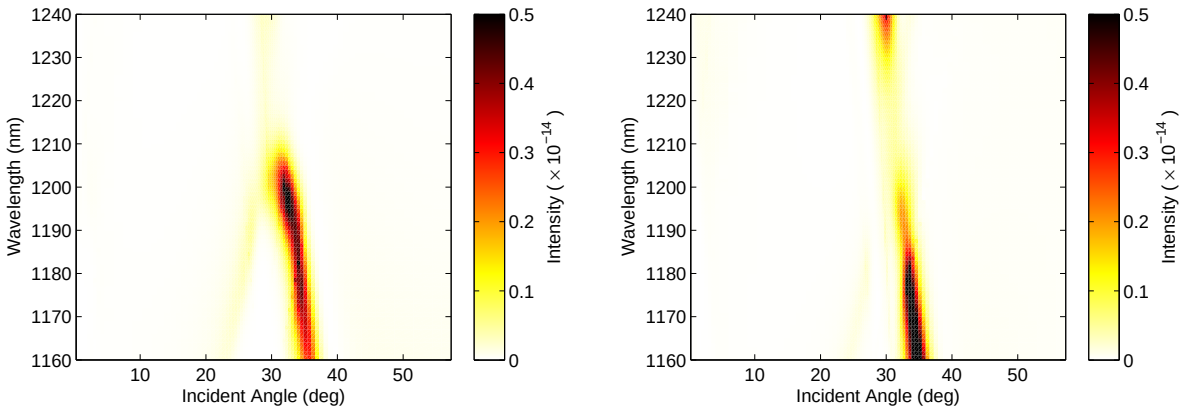

(a) (b)

Figure 7: The total transmitted SHG intensity as a function of incident angle and incident wavelength for Au grating slab with (a) rectangular and (b) trapezoidal groove profiles.